# Controls-Oriented Model for Secondary Effects of Wake Steering

Jennifer King[1], Paul Fleming[1], Ryan King[1], Luis A. Martínez-Tossas[1], Christopher J. Bay[1],
Rafael Mudafort[1], and Eric Simley[1]

[1]National Wind Technology Center, National Renewable Energy Laboratory, Golden, CO, 80401, USA

*Correspondence to:* Jennifer King (jennifer.king@nrel.gov)

**Abstract.** This paper presents a model to incorporate the secondary effects of wake steering in large arrays of turbines. Previous models have focused on the aerodynamic interaction of wake steering between two turbines. The model proposed in this paper builds on these models to include yaw-induced wake recovery and secondary steering seen in large arrays of turbines when wake steering is performed. Turbines operating in yaw misaligned conditions generate counter-rotating vortices that entrain momentum and contribute to the deformation and deflection of the wake at downstream turbines. Rows of turbines can compound the effects of wake steering that benefit turbines far downstream. This model quantifies these effects and demonstrates that wake steering has greater potential to increase the performance of a wind farm due to these counter-rotating vortices especially for large rows of turbines. This is validated using numerous large eddy simulations for two-turbine, three-turbine, five-turbine, and wind farm scenarios.

## 1 Introduction

Wake steering is a type of wind farm control in which wind turbines in a wind farm operate with an intentional yaw misalignment to mitigate the effects of its wake on downstream turbines in order to increase overall combined wind farm energy production (Wagenaar et al. (2012)). To design model-based controllers for wake steering, engineering models of the aerodynamic interactions between turbines are needed. Engineering models, in this context, are computationally efficient models that include enough physics to predict wake steering behavior while running fast enough to be optimized in real-time. These models can then be used in the design of wind farm control strategies (Simley et al. (2019); Fleming et al. (2019a)), layout optimizations (Gebraad et al. (2017); Stanley and Ning (2019)), or real-time control (Annoni et al. (2019)).

An early model of wake steering was provided in Jiménez et al. (2010). This model was combined with the Jensen model (Jensen (1984)) in the multi-zone wake model in FLORIS (Gebraad et al. (2016)). The model was compared with large-eddy simulations (LES) using the Simulator for Wind Farm Applications (SOWFA, Churchfield et al. (2014)) and several additional corrections including division of the wake into separate zones were added to better capture the aerodynamic interactions.

Several recent papers proposed a new wake deficit and wake deflection model based on Gaussian self-similarity (Bastankhah and Porté-Agel (2014, 2016); Niayifar and Porté-Agel (2015); Abkar and Port-Agel (2015)). This model includes added turbulence due to the turbine operation that influences wake recovery. In addition, this model has minimal tuning parameters and includes atmospheric parameters that can be measured such as turbulence intensity (Niayifar and Porté-Agel (2015)). This model is commonly referred to as the Bastankah model, EPFL model, or Gaussian model. We will use the term Gaussian for

the remainder of the paper. The Gaussian model was included as a wake model within the FLORIS tool (NREL (2019)). It has been used to design a controller for a field campaign in Fleming et al. (2019a), study wake steering robustness (Simley et al. (2019)), and has been validated with lidar measurements (Annoni et al. (2018)). The Gaussian model is also used in wind farm design optimization in Stanley and Ning (2019).

5    One of the main issues observed with the Gaussian model in FLORIS is that the model tends to under-predict gains in power downstream with respect to LES and field data. In addition, Fleming et al. (2016) and Schottler et al. (2016) show wake steering is asymmetrical, i.e., clockwise and counter-clockwise yaw rotations do not produce equal benefits at the downstream turbine.

Fleming et al. (2018a) investigates the importance of considering explicitly the counter-rotating vortices generated in wake steering (Medici and Alfredsson (2006); Howland et al. (2016); Vollmer et al. (2016)) to fully describe wake steering in
10   engineering models. These vortices deflect and deform the wake at the downstream turbine. It is also noted in Fleming et al. (2018a) that these vortices persist farther downstream and impact turbines that are third, fourth, etc. in the row. This is known as secondary steering. It was proposed that modeling the counter-rotating vortices generated in wake steering could provide a means to model this process and how wake steering will function when dealing with larger turbine arrays. Further, Ciri et al. (2018), has shown that modeling/accounting for the size of these vortices versus the length-scales in the atmospheric boundary
15   layer explain variations of performance of wake steering for differently sized rotors.

Martínez-Tossas et al. (2019) provides a wake model, known as the curl model, which explicitly models these vortices. The paper shows that modeling the vortices can predict the deflection of the wake in misaligned conditions as well as the change in wake shape and cross-stream flows observed in Medici and Alfredsson (2006); Howland et al. (2016); Vollmer et al. (2016); Fleming et al. (2018a). However, the RANS-like implementation of the curl model, and flow-marching simulation solution
20   significantly increases the computation complexity (around 1000x).

This paper presents a hybrid wake model, which modifies the Gaussian model (Bastankhah and Porté-Agel (2014, 2016); Niayifar and Porté-Agel (2015)), with analytic approximations made of the curl model in (Martínez-Tossas et al. (2019)). This hybrid model will be referred to as the Gauss-Curl Hybrid, or GCH model. We propose it as a compromise which maintains the many advantages of the Gaussian model, while incorporating corrections to address the following three important
25   discrepancies:

1. Vortices drive a process of added yaw-based wake recovery, which increases the gain from wake steering to match LES and field results.

2. The interaction of the counter-rotating vortices with the atmospheric boundary layer shear layer and wake rotation induces wake asymmetry naturally.

30   3. By modeling of the vortices, secondary-steering and related multi-turbine effects are included.

In this paper, we will introduce the analytical modifications made to the Gaussian model in Section 2. We will use numerous LES simulations to show that the the improvements made in GCH resolves the discrepancies identified above. This model will demonstrate how it compares with LES of two-turbines (Section 3), three turbines (Section 4), five turbines (Section 5), and a

38-turbine wind farm (Section 6). In addition to these simulations, the proposed model is also validated using the results of a wake steering field campaign at a commercial wind farm (Fleming et al. (2019b)).

## 2   Controls-Oriented Model

This section briefly describes the Gaussian model used to describe the velocity deficit and the effects of wake steering in a wind farm. The proposed model builds upon the Gaussian model introduced in Bastankhah and Porté-Agel (2016); Abkar and Porté-Agel (2014); Abkar and Port-Agel (2015); Niayifar and Porté-Agel (2015) by including entrainment, asymmetry, and secondary wake steering effects seen in LES as well as field results.

### 2.1   Velocity Deficit Model

The wind turbine wake model used to characterize the velocity deficit behind a turbine in normal operation in a wind farm was introduced by several recent papers including Bastankhah and Porté-Agel (2016); Abkar and Port-Agel (2015); Niayifar and Porté-Agel (2015); Bastankhah and Porté-Agel (2014). The velocity deficit of the wake is computed by assuming a Gaussian wake, which is based on self-similarity theory often used in free shear flows (Pope (2001)). An analytical expression for the three-dimensional velocity, $u_G$, behind a turbine is computed as:

$$\frac{u_G(x,y,z)}{U_\infty} = 1 - Ce^{-(y-\delta)^2/2\sigma_y^2 - (z-z_h)^2/2\sigma_z^2} \tag{1}$$

$$C = 1 - \sqrt{1 - \frac{(\sigma_{y0}\sigma_{z0})M_0}{\sigma_y\sigma_z}} \tag{2}$$

$$M_0 = C_0\left(2 - C_0\right) \tag{3}$$

$$C_0 = 1 - \sqrt{1 - C_T} \tag{4}$$

where $C$ is the velocity deficit at the wake center, $U_\infty$ is the freestream velocity, $\delta$ is the wake deflection (see Section 2.1.1), $z_h$ is the hub height of the turbine, $\sigma_y$ defines the wake width in the $y$ direction, and $sigma_z$ defines the wake width in the $z$ direction. Each of these parameters are defined with respect to each turbine. The subscript "0" refers to the initial values at the start of the far wake, which is dependent on ambient turbulence intensity, $I_0$, and the thrust coefficient, $C_T$. For additional details on near-wake calculations, the reader is referred to Bastankhah and Porté-Agel (2016). Abkar and Port-Agel (2015) demonstrate that $\sigma_y$ and $\sigma_z$ grow at different rates based on lateral wake meandering ($y$ direction) and vertical wake meandering ($z$ direction). The velocity distributions $\sigma_z$ and $\sigma_y$ are defined as:

$$\frac{\sigma_z}{D} = k_z\frac{(x-x_0)}{D} + \frac{\sigma_{z0}}{D} \quad \text{where} \quad \frac{\sigma_{z0}}{D} = \frac{1}{2}\sqrt{\frac{u_R}{U_\infty + u_0}} \tag{5}$$

$$\frac{\sigma_y}{D} = k_y \frac{(x-x_0)}{D} + \frac{\sigma_{y0}}{D} \quad \text{where} \quad \frac{\sigma_{y0}}{D} = \frac{\sigma_{z0}}{D} \cos\gamma \tag{6}$$

where $D$ is the rotor diameter, $u_R$ is the velocity at the rotor, $u_0$ is the velocity behind the rotor, $k_y$ defines the wake expansion in the lateral direction, and $k_z$ defines the wake expansion in the vertical direction. For this study, $k_y$ and $k_z$ are set to be equal
5  and the wake expands at the same rate in the lateral and vertical directions. The wakes are combined using the traditional sum of squares method (Katić et al. (1986)), although alternate methods are proposed in Niayifar and Porté-Agel (2015).

### 2.1.1 Wake Deflection

In addition to the velocity deficit, a wake deflection model is used to describe the turbine behavior in yaw misaligned conditions which occur when performing wake steering and is also implemented based on Bastankhah and Porté-Agel (2016). The angle
10  of wake deflection, $\theta$, due to yaw misalignment is defined as:

$$\theta \approx \frac{0.3\gamma}{\cos\gamma} \left(1 - \sqrt{1 - C_T \cos\gamma}\right) \tag{7}$$

The initial wake deflection, $\delta_0$, is then defined as:

$$\delta_0 = x_0 \tan\theta \tag{8}$$

where $x_0$ indicates the length of the near wake, which is typically on the order of 3 rotor diameters. This can be computed
15  analytically based on Bastankhah and Porté-Agel (2016).

The total deflection of the wake due to yaw misalignment is defined as:

$$\delta = \delta_0 + \frac{\gamma E_0}{5.2}\sqrt{\frac{\sigma_{y0}\sigma_{z0}}{k_y k_z M_0}} \ln\left[\frac{\left(1.6 + \sqrt{M_0}\right)\left(1.6\sqrt{\frac{\sigma_y \sigma_z}{\sigma_{y0}\sigma_{z0}}} - \sqrt{M_0}\right)}{\left(1.6 - \sqrt{M_0}\right)\left(1.6\sqrt{\frac{\sigma_y \sigma_z}{\sigma_{y0}\sigma_{z0}}} + \sqrt{M_0}\right)}\right] \tag{9}$$

where $E_0 = C_0^2 - 3e^{\frac{1}{12}}C_0 + 3e^{\frac{1}{3}}$. See Bastankhah and Porté-Agel (2016) for details on the derivation.

### 2.2 Spanwise and Vertical Velocity Components

20  The spanwise and vertical velocity components are currently not computed in the Gaussian model, but they are a critical component for modeling the effects of wake steering. These velocity components can be computed based on wake rotation and yaw misalignment as shown in Martínez-Tossas et al. (2019) and Bay et al. (2019).

Wake rotation is included by modeling the effects of rotation using a Lamb-Oseen vortex to de-singularize the behavior near the center of the rotor. The circulation strength for the wake rotation vortex is now:

25  $$\Gamma_{\text{wr}} = \frac{\pi(a - a^2)U_\infty D}{\lambda} \tag{10}$$

where $a$ is the axial induction factor of the turbine and $\lambda$ is the tip-speed ratio. See Martínez-Tossas et al. (2019) for additional details.

The vertical and spanwise velocities can then be computed using the strength of the vortex, $\Gamma$, by:

$$V_{\text{wake rotation}} = \frac{\Gamma_{\text{wr}}(y-y_0)}{2\pi\left((y-y_0)^2+(z-z_h)^2\right)}\left(1-e^{\frac{-((y-y_0)^2-(z-z_h))^2}{\epsilon^2}}\right) \tag{11}$$

$$W_{\text{wake rotation}} = \frac{\Gamma_{\text{wr}}(z-z_h)}{2\pi\left((y-y_0)^2+(z-z_h)^2\right)}\left(1-e^{\frac{-((y-y_0)^2-(z-z_h))^2}{\epsilon^2}}\right) \tag{12}$$

where $y_0$ is the spanwise position of the turbine, $\epsilon$ represents the size of the vortex core. In this paper, $\epsilon = 0.3D$.

5    In addition to the wake rotation, when a turbine is operating in yaw-misaligned conditions, the turbine generates counter-rotating vortices that are released at the top and the bottom of the rotor. This is an approximation to the counter-rotating vortices defined in Martínez-Tossas et al. (2019) in that this model approximates the vortices as one at the top and bottom of the rotor rather than a collection of smaller vortices. This is similar to what is done in Shapiro et al. (2018). The strength of these vortices can be computed as, $\Gamma$, and is a function of the yaw angle, $\gamma$, (Martínez-Tossas et al. (2019)):

10    $$\Gamma(\gamma) = \frac{\pi}{8}\rho D U_\infty C_T \sin\gamma\cos\gamma^2 \tag{13}$$

where $\rho$ is the air density.

As is done with wake rotation, The spanwise $V$ and vertical $W$ velocity components can be computed based on the strength of the wake rotation and yaw misalignment of a turbine. The spanwise velocity can be computed as:

$$V_{\text{top}} = \frac{\Gamma(y-y_0)}{2\pi\left((y-y_0)^2+(z-(z_h+R))^2\right)}\left(1-e^{\frac{-((y-y_0)^2-(z-(z_h+R)))^2}{\epsilon^2}}\right) \tag{14}$$

$$V_{\text{bottom}} = \frac{\Gamma(y-y_0)}{2\pi\left((y-y_0)^2+(z-(z_h-R))^2\right)}\left(1-e^{\frac{-((y-y_0)^2-(z-(z_h-R)))^2}{\epsilon^2}}\right) \tag{15}$$

where $R$ is the turbine radius and $V_{\text{top}}$ and $V_{\text{bottom}}$ are the spanwise velocities generated at the top and bottom of the rotor. The spanwise and vertical velocities are combined using a linear combination at downstream turbines as is done in Martínez-Tossas et al. (2015); Bay et al. (2019). The total spanwise velocity is:

20    $$V_{\text{wake}} = V_{\text{top}} + V_{\text{bottom}} + V_{\text{wake rotation}} \tag{16}$$

Similarly, the vertical velocity can be written as:

$$W_{\text{top}} = \frac{\Gamma_{\text{top}}(z-(z_h+R))}{2\pi\left((y-y_0)^2+(z-(z_h+R))^2\right)}\left(1-e^{\frac{-((y-y_0)^2-(z-(z_h+R)))^2}{\epsilon^2}}\right) \tag{17}$$

$$W_{\text{bottom}} = \frac{\Gamma_{\text{bottom}}(z-(z_h-R))}{2\pi\left((y-y_0)^2+(z-(z_h-R))^2\right)}\left(1-e^{\frac{-((y-y_0)^2-(z-(z_h-R)))^2}{\epsilon^2}}\right) \tag{18}$$

The total vertical velocity can be computed as:

$$W_{\text{wake}} = W_{\text{top}} + W_{\text{bottom}} + W_{\text{wake rotation}} \tag{19}$$

Note, ground effects are included by adding mirrored vortices below the ground as is done in Martínez-Tossas et al. (2019).

Finally, the vortices generated by the turbines decay as they move downstream. The dissipation of these vortices is described
5   in Bay et al. (2019) and can be computed as:

$$V = V_{\text{wake}} \left( \frac{\epsilon^2}{4\nu_T \frac{(x-x_0)}{U_\infty} + \epsilon^2} \right) \tag{20}$$

$$W = W_{\text{wake}} \left( \frac{\epsilon^2}{4\nu_T \frac{(x-x_0)}{U_\infty} + \epsilon^2} \right) \tag{21}$$

where $\nu_T$ is the turbulent viscosity, which is defined using a mixing length model:

10   $$\nu_T = l_m^2 \left| \frac{\partial U}{\partial z} \right| \tag{22}$$

where $l_m = \frac{\kappa z}{1 + \kappa z/\lambda_T}$, $\kappa = 0.41$, and $\lambda_T = D/8$. $\lambda_T$ is the value of the mixing length in the free atmosphere (Martínez-Tossas et al. (2019)).

### 2.3   Added Wake Recovery due to Yaw Misalignment

The streamwise velocity and the wake deflection are influenced by these velocity components, $V$ and $W$. First, the wake
15   recovers more when the turbine is operating in misaligned conditions due to the large-scale entrainment of flow into the wind
farm domain. In this paper, we include added wake recovery that is assumed to be primarily due to added entrainment from the
presence of vertical velocity, $W$. Using a control volume approach for momentum conservation, the modified wake velocity,
$u$, can be computed by adding an additional wake recovery component to the Gaussian model:

$$u(x,y,z) = u_G(x,y,z) + \underbrace{\frac{W(x,y,z)(x-x_0)(y-y_0)}{\pi \left( \alpha_r(x-x_0) + \frac{D}{2} \right)^2}}_{\text{added velocity from yaw}} \tag{23}$$

20   where $u_G$ is computed by (1), $W$ is computed by (21), i.e., the vertical velocity generated by wake rotation and the counter-
rotating vortices present when a turbine is operating in misaligned conditions, $\alpha_r$ is a tuning parameter that dictates how much
the entrainment affects the wake recovery. For this paper, that term is set to $\alpha_r = 0.03$. The larger $\alpha_r$ is the smaller the effect
of entrainment is on the streamwise velocity component.

### 2.3.1   Secondary Steering through Effective Yaw

25   In addition to added wake recovery, the model proposed in this paper is able to predict secondary steering. The wake deflection
model described in Section 2.1.1 can be used to describe the deflection of the wake for a two turbine case. However, additional

information is needed to describe the impact of yaw misalignment on turbines in large wind farms as is shown in Fleming et al. (2018a).

Specifically, the vortices described in the previous section propagate far downstream, dissipate, and affect all turbines directly downstream of the turbine that generated the vortices. When they reach a downstream turbine, they impact the wake of the

5 downstream turbine in a phenomenon called secondary steering (Fleming et al. (2018b)). The spanwise and vertical velocities generated by the counter-rotating vortices act like an effective yaw angle at the next turbine. In other words, the spanwise and vertical velocities of upstream turbines affect the deformation and deflection of a wake downstream as if the downstream turbine were implementing wake steering even when it is aligned with the flow. This can be approximated as an apparent or effective yaw angle. To model secondary steering, an effective yaw angle is computed to describe the effect of the vortices

10 generated at the upstream turbine on the downstream turbine wake. The effective yaw angle is computed using the spanwise velocity, $V$, present at the turbine rotor, which contributes to an effective circulation that is responsible for deflecting and deforming the wake. At a downstream turbine, the strength of the effective circulation, $\Gamma_{\text{eff}}$ is calculated by taking the inverse of (20):

$$\Gamma_{\text{eff}} = \frac{1}{N} \sum_{i}^{N} \left| \frac{2\pi V_i \left((y_i - y_0)^2 + (z_i - z_h)^2\right)}{(y_i - y_0) \left(1 - e^{\frac{-((y_i - y_0)^2 - (z_i - z_h))^2)}{\epsilon^2}}\right)} \right| \tag{24}$$

15 where $V$ is spanwise velocities inside the rotor area and $N$ is the number of points in the rotor area. The effective yaw angle, $\gamma_{\text{eff}}$, is then computed using $\Gamma_{\text{eff}}$ and solving for $\gamma$ in (13). The total wake deflection can be computed using (9) where the total yaw angle, $\gamma$ is:

$$\gamma = \gamma_{\text{turb}} + \gamma_{\text{eff}} \tag{25}$$

where $\gamma_{\text{turb}}$ is the amount of yaw offset the turbine is actually applying. This $\gamma$ is used in (9) to compute the lateral deflection

20 of the wake.

Due to the presence of the effective yaw angle, downstream turbines generally do not have to yaw as much as upstream turbines to produce large gains. This phenomenon was observed in a wind tunnel study (Bastankhah and Porté-Agel (2019)).

## 3 Two-Turbine Analysis

In this section, SOWFA simulations were run for a variety of two-turbine scenarios. Each two-turbine scenario is run using both the Gaussian and the GCH model. Note, the effects of secondary steering will have no effect on two-turbine scenarios, and therefore GCH is equivalent to only the yaw-added recovery (YAR) effect addressed in Section 2.3. Therefore, we will

5  refer to the model as YAR in this section. This analysis focuses on a wind speed of 8 m/s with turbulence intensities of 6% and 10% TI, where spacing between the turbines is fixed at 7D. It should be noted that the Gaussian model and the GCH model share the same tuning parameters and have been tuned to the same value, which is consistent with what has previously been published in literature. Only turbulence intensity and freestream velocity are changed between simulations to match large eddy simulation. Mean wind speeds vary slightly between low and high turbluence scenarios, e.g. $U_\infty = 8.34$ m/s for low turbulence

10  and $U_\infty = 8.38$ m/s for high turbulence cases.

The first turbine is fixed at one location, while its yaw angle is varied through a range of positive (CCW) and negative (CW) yaw offsets. The second turbine is always aligned the flow, but is moved between -R,0,+R offset laterally from the upstream turbine. The SOWFA simulations with the front turbines yawed +20 are illustrated in Fig. 1 (right column). Fig. 1 also shows cases with no yaw (middle column) and with -20° offset (left column). Simulations with +R offset are in the top row, 0R offset

15  are in the middle row, and -R offset are in the bottom row.
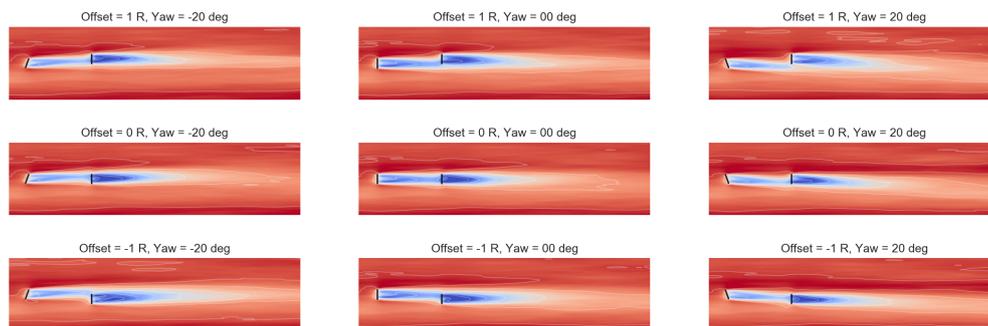
**Figure 1.** Flow fields of streamwise velocity components for when the second turbine is offset +R (top), 0R or aligned (middle), and -R (bottom). The front turbine is yawed $-20°$ (left column), $0°$ (middle column), and $+20°$ (right column)

The results are analyzed by considering the percentage gain (or loss) in power of the second turbine from yawing the front turbine in each case either +20° (CCW) or -20° (CW). These results are shown in Fig. 2. Most of the improvements in GCH are expected to mainly benefit larger arrays of turbine scenarios where secondary steering plays a role. However, the suggested improvements in YAR can be seen in the asymmetry introduced by wake rotation and shear. This can be seen most clearly in

20  the aligned 0R cases (middle row of Fig. 2). The initial Gaussian model assumes the gain on the second turbine is equivalent

whether yawing positive or negatively, whereas YAR matches the pattern from SOWFA that the positive gains exceed the negative.
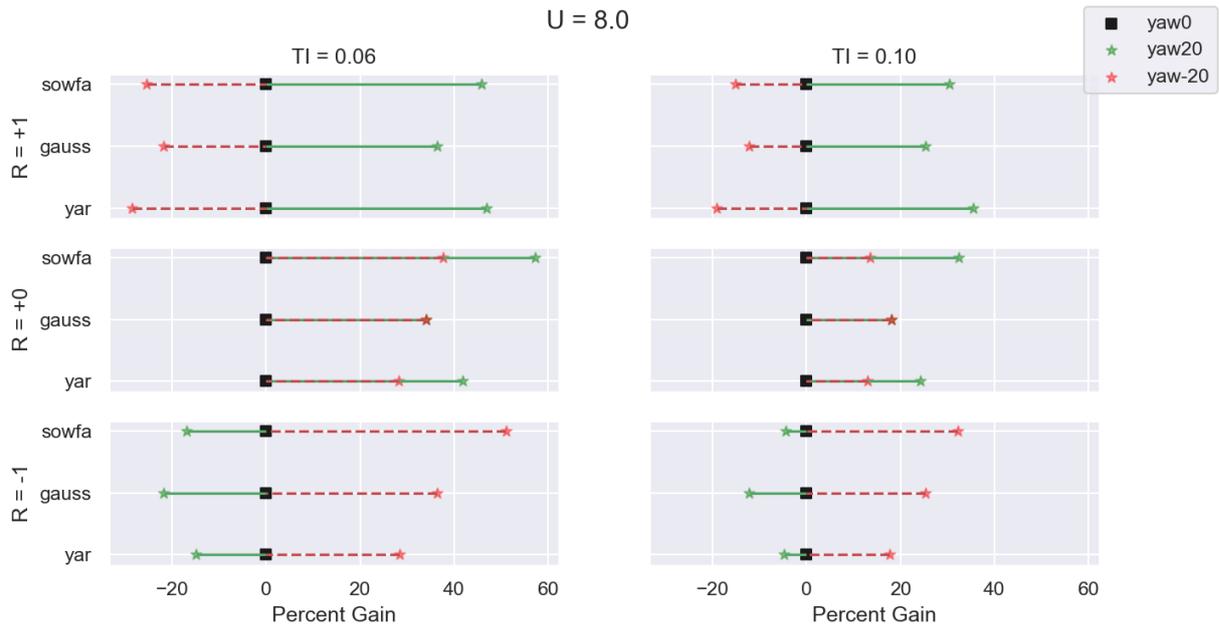
**Figure 2.** Results for percent change of power in the second turbine in each offset location, for each of model, at 8 m/s and 6% turbulence intensity (left) and 10% turbulence intensity (right). The results are shown where the second turbine is offset +R (top row), 0R (middle row), and -R (bottom row).

The second improvement focuses on the magnitude of gains from positive yawing. For the four cases shown in Fig. 2 in which positive yawing is beneficial according to SOWFA, the Gaussian model significantly underestimates the gain in all cases.

5 Further, considering the case in which positive yaw is harmful, -R, the Gaussian consistently over-estimates the loss, while the YAR model more closely matches SOWFA by producing less negative results. However, it is noted that YAR does not perform as well as the Gaussian model when predicting the gains of negative yaw when the second turbine is offset by -R. This will be subject to future research. It should also be noted that a loads study of wake steering suggested that positive yaw angles are less harmful to turbines and thus mainly positive angles are used for wake steering (Damiani et al. (2017)).

# 4 Three-Turbine Analysis

Next, the Gaussian model, GCH model, and SOWFA are compared in three-turbine array simulations. The three-turbine array demonstrates the benefits of yaw-added recovery (YAR) effect as well as secondary steering (SS). The following plots show the contributions of YAR and SS compared with the Gaussian model and the full GCH model, which contains both YAR and SS.

5 The YAR and SS models are computed by disabling the model produced in Section 2.3 and Section 2.3.1 respectively within the GCH model to isolate the two effects.
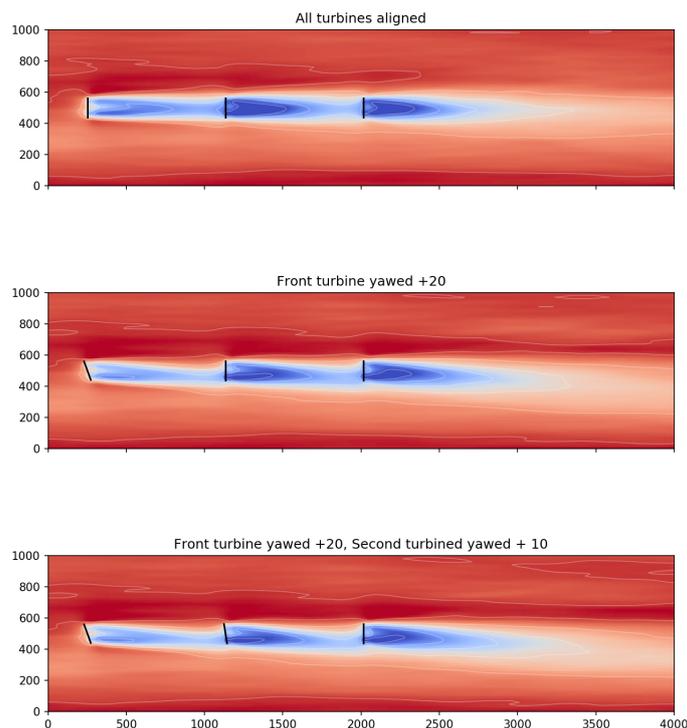
**Figure 3.** Three-turbine array in SOWFA where all turbines are aligned (top), the first turbine is yawed +20° (middle), and the first turbine is yawed +20° and the second turbine is yawed +10°.

The three turbine scenario was simulated at 8 m/s with 6% and 10% turbulence intensities and spaced $7D$ apart in the streamwise direction. Fig. 3 shows the flow fields from the SOWFA simulations for baseline (top row), the first turbine yawed 20° (middle row), and the first turbine yawed 20° and the second turbine yawed 10° (bottom row). For visual comparison,
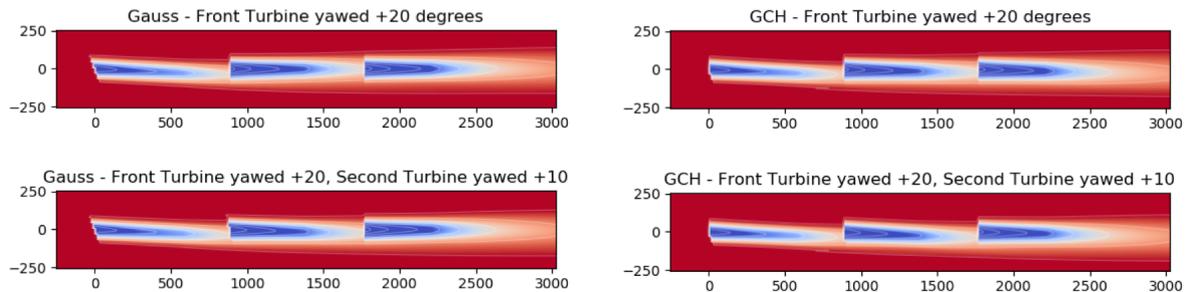
**Figure 4.** FLORIS results for the three-turbine case shown for the Gaussian model (left) and the GCH model (right), where the first turbine is yawed $20°$ (top row) and the first turbine is yawed $20°$ and the second turbine is yawed $10°$ (bottom row).

Fig. 4 shows the Gaussian model (left) and the GCH model (right) where the first turbine is yawed $20°$ (top row) and the first turbine is yawed $20°$ and the second turbine is yawed $10°$ (bottom row). Visually, the impact of secondary steering can be seen on the wake of the third turbine in the GCH model (right column), i.e. the wake of the third turbine is slightly deflected (downward in this plotting orientation) even though the third turbine is not operating in misaligned conditions.

5     Next, several simulations were run at each turbulence intensity where the first turbine was yawed $20°$ and the second turbine was yawed between $-20°$ and $+20°$. Figure 5 and 6 shows the relative power gains of the SOWFA simulations for turbulence intensities of 6% and 10% respectively relative to a baseline case of all turbines aligned. The SOWFA simulations are compared with the Gaussian model, YAR, SS, and the GCH model. The turbines in the three turbine cases are labeled as Turbine 1 (most upstream turbine), Turbine 2 (middle turbine), and Turbine 3 (most downstream). The power gains of Turbine 2 are shown in

10    the left plot in Figs. 5 and 6, Turbine 3 is shown in the middle plot, and the total power gains are shown in the right plot.

    The Gaussian model is not able to capture the secondary effects of wake recovery and secondary steering. The Gaussian model is able to capture gains in low turbulence (6%) conditions, see Fig. 5. However, it does not see any gains when turbulence intensity is higher as shown Fig. 6. It is also important to note that for Turbine 3 and the total gains, the Gaussian model forecasts a change in power which is symmetrical about changes in Turbine 2, whereas SS and the GCH model predict that a $-10°$ yaw

15    on a turbine, which is behind a turbine yawed $+20°$ is counter-productive, while a complementary $+10°$ yaw is more valuable than either Gauss or YAR would predict. The figures also show how the two added effects, YAR and SS, complement each other. YAR improves the prediction of the middle Turbine 2, while SS can only improve the predictions farther downstream. The combined GCH model is most like LES in both low and high turbulence scenarios.
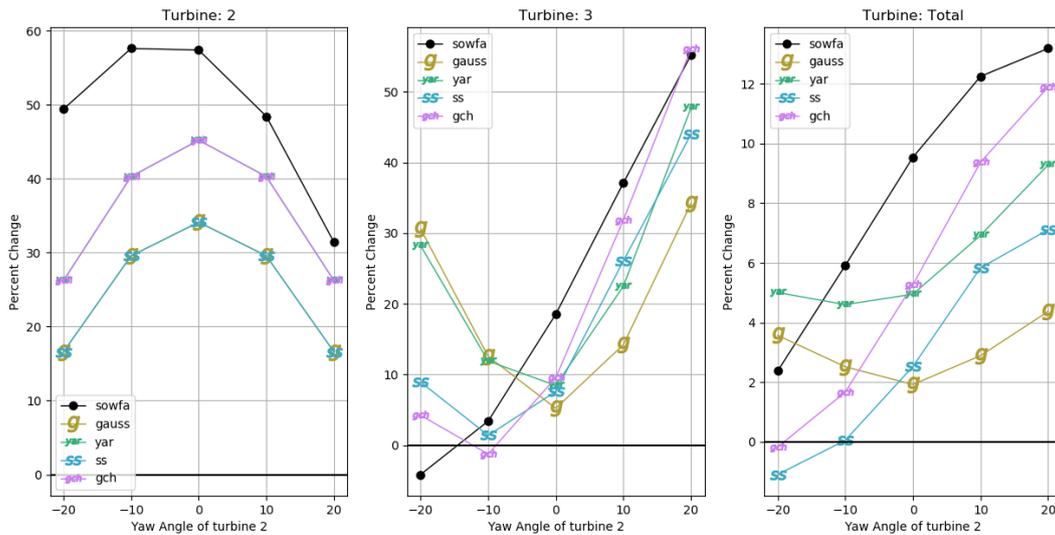
**Figure 5.** Comparison of changes in power when sweeping the angle of the second turbine, i.e. Turbine 2, when the angle of the first turbine, i.e., Turbine 1 is set to +20° where the wind speed was 8 m/s and the turbulence intensity was 6%. The results of the change in power of the third turbine, as well as the overall total of all three turbines, reflect the importance that the two yaw offsets are in the same direction.
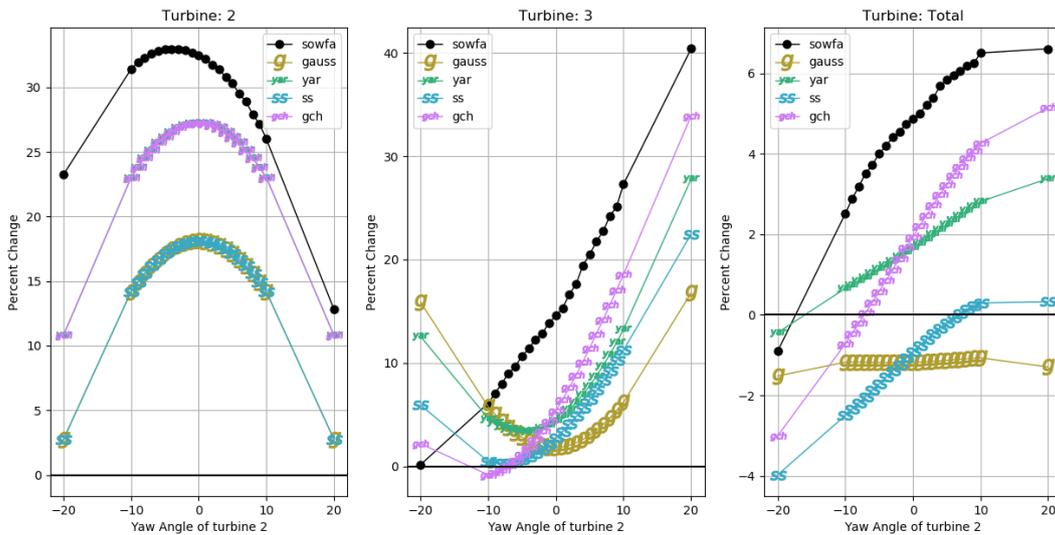
**Figure 6.** Comparison of changes in power when sweeping the angle of the second turbine, i.e. Turbine 2, when the angle of the first turbine, i.e., Turbine 1 is set to +20° where the wind speed was 8 m/s and the turbulence intensity was 10%.
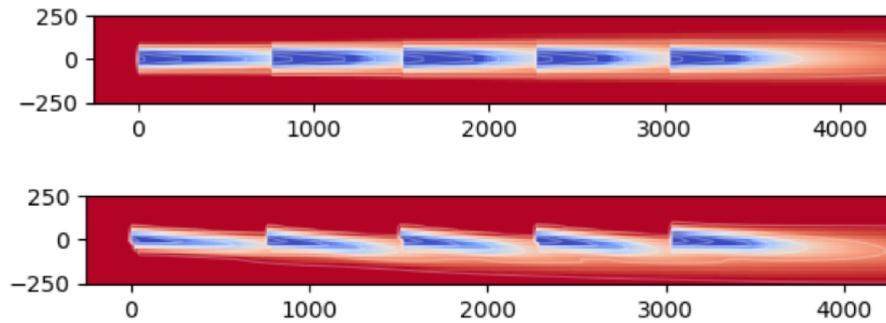
**Figure 7.** Flow field of 5 turbines using GCH for the baseline case (top) and the optimized case (bottom). The optimized yaw angles are based on the values shown in Table 1.

## 5   Five-Turbine Analysis

Next, five turbines were simulated in SOWFA, the Gaussian model, and the GCH model for different combinations of yaw angles, starting with all aligned, the first turbine yawed $25°$, the first and second turbine yawed $25°$, and the first three turbines yawed $25°$. Fig. 7 shows the flow field for GCH in baseline conditions (top) and optimized conditions (bottom). The five turbine

5   array was simulated with a wind speed of 8 m/s and turbulence intensities of 6% (labeled as low turbulence) and 10% (labeled as high turbulence). The turbines are spaced $6D$ in the streamwise direction.

Fig. 8 shows the absolute powers of each turbine in the five turbine array, excluding the first turbine, for low turbulence conditions. The GCH model is able to most closely capture the trends seen in SOWFA especially when evaluating total turbine power. The power gains for each turbine are shown in Fig. 9. The Gaussian model is pessimistic about the potential gains for

10   the five turbine case. YAR and SS both contribute significantly to the total gains seen in the five turbine case. It should be noted that all models have a difficult time predicting the absolute power and the power gain of the last turbine. This may be resolved with a more rigorous "turbulence" model than the one used in this model, see Annoni et al. (2018). In addition, this model does not directly account for deep array effects and this may also be a source of error and is a subject of ongoing research.

Fig. 10 shows the same five turbine analysis for the high turbulence scenario (10% turbulence intensity). Again, the GCH

15   model most closely follows the trends seen in SOWFA. The most notable difference between GCH and the Gaussian model is that the Gaussian model is extremely pessimistic about wake steering in high turbulence, i.e., there are no gains to be realized under these conditions. However, according to SOWFA, large gains are still expected from wake steering even in high turbulence. The GCH model is able to capture the power gains seen in SOWFA at high turbulence intensities although GCH is still slightly under-predicting the potential gains of wake steering.
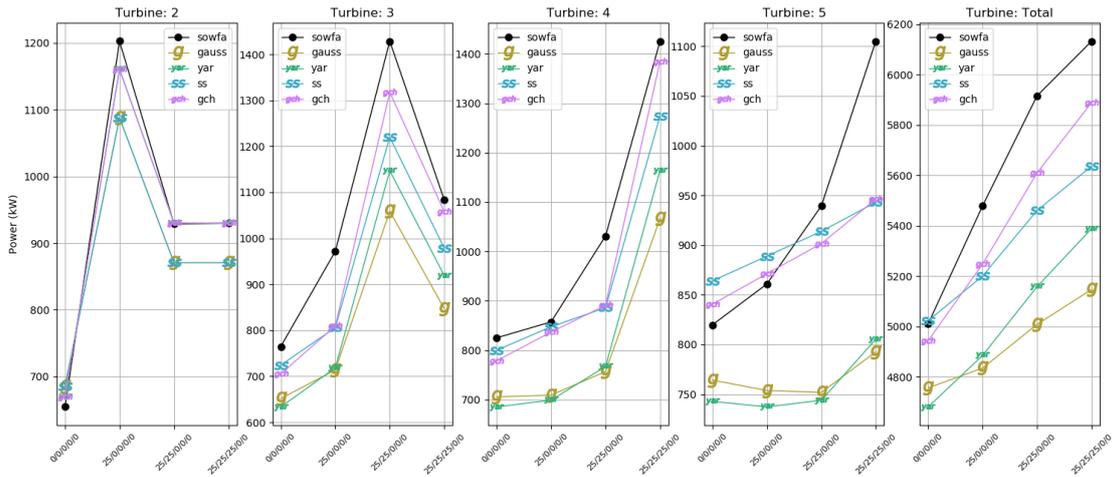
**Figure 8.** Absolute power values for each turbine (excluding the upstream turbine 1) in the five turbine array for a wind speed of 8 m/s and low turbulence, i.e., 6% turbulence intensity. Total turbine power is shown in the far right plot. The $x$-axis shows the combination of yaw angles plotted.
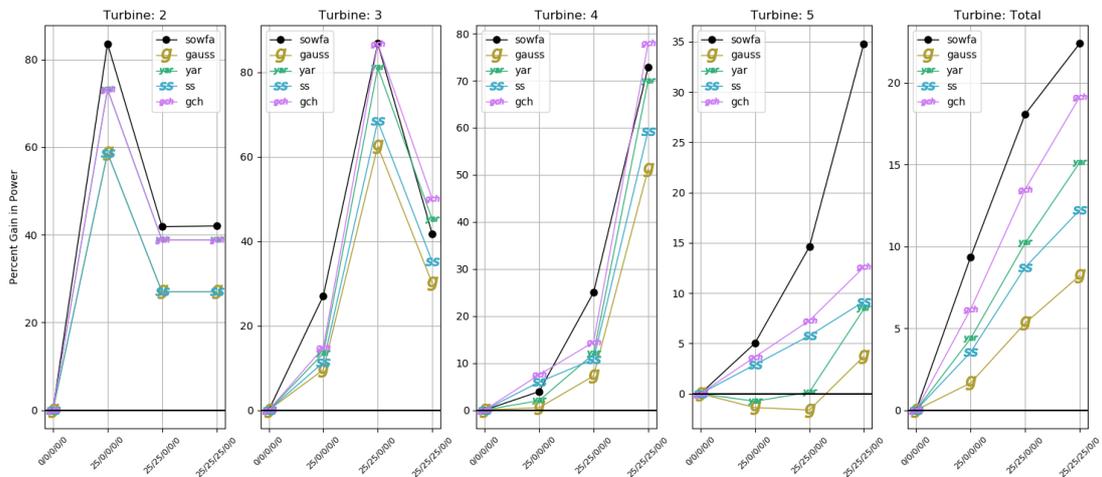
**Figure 9.** Power gains for each turbine (excluding the upstream turbine 0) in the five turbine array for a wind speed of 8 m/s and low turbulence, i.e., 6% turbulence intensity. Total power gain is shown in the far right plot. The $x$-axis shows the combination of yaw angles plotted.
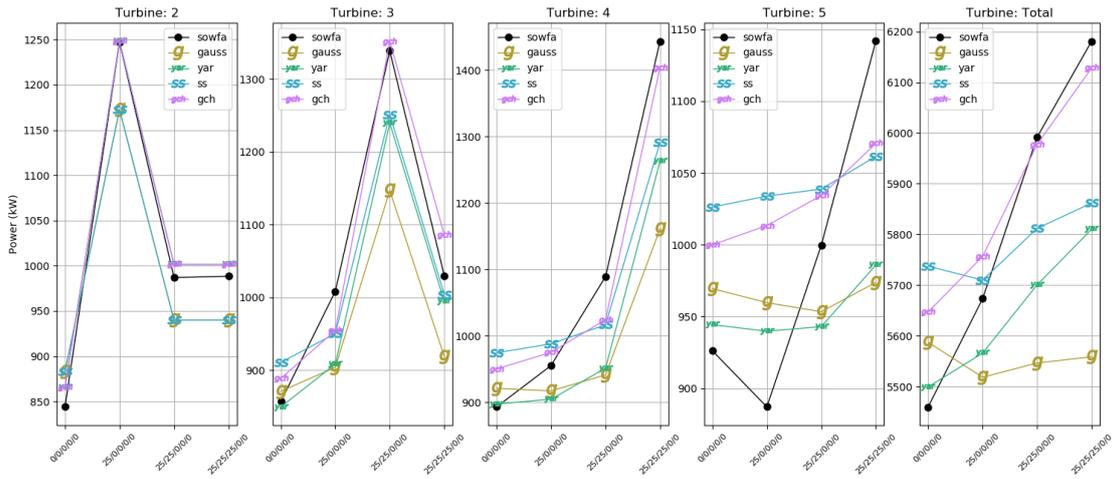
**Figure 10.** Absolute power values for each turbine (excluding the upstream turbine) in the five turbine array for a wind speed of 8 m/s and high turbulence, i.e., 10% turbulence intensity. Total turbine power is shown in the far right plot. The $x$-axis shows the combination of yaw angles plotted.
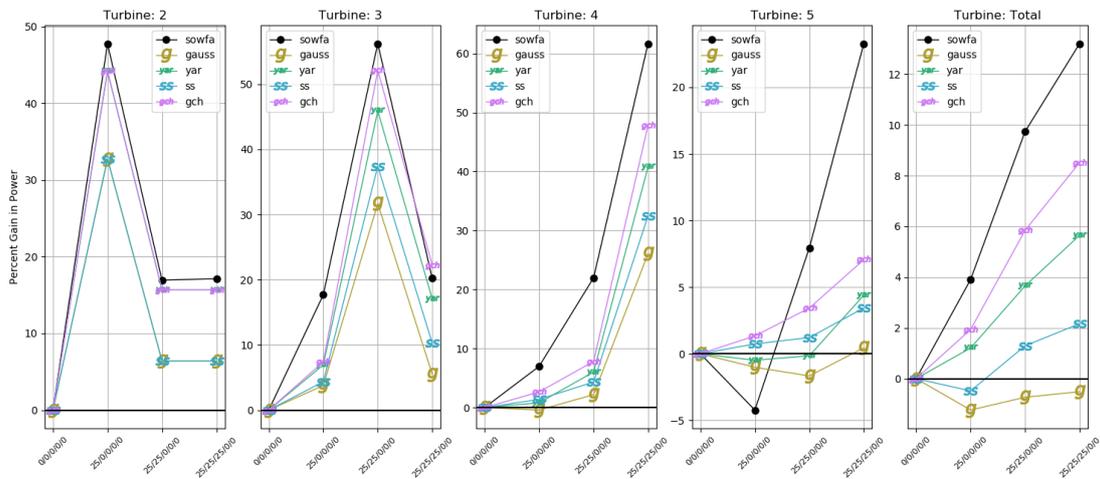
**Figure 11.** Power gains for each turbine (excluding the upstream turbine) in the five turbine array for a wind speed of 8 m/s and high turbulence, i.e., 10% turbulence intensity. Total power gain is shown in the far right plot. The $x$-axis shows the combination of yaw angles plotted.

| Case | Turbine 1 | Turbine 2 | Turbine 3 | Turbine 4 | SOWFA Gain | Gauss Gain | GCH Gain |
|---|---|---|---|---|---|---|---|
| Low Turbulence | | | | | | | |
| Gauss optimized angles | 24.0 | 25.0 | 25.0 | 25.0 | 22.7% | 9.9% | 23.1% |
| GCH optimized angles | 25.0 | 25.0 | 22.1 | 18.7 | **23.7%** | 9.4% | 23.5% |
| Max yaw angles | 25.0 | 25.0 | 25.0 | 25.0 | 22.9% | 9.8% | 23.3% |
| High Turbulence | | | | | | | |
| Gauss optimized angles | 12.9° | 23.4° | 19.7° | 14.1° | 7.5% | 1.2% | 9.2% |
| GCH optimized angles | 24.2 | 24.4 | 22.7 | 16.5 | **14.3%** | -0.2% | 11.0% |
| Max yaw angles | 25.0 | 25.0 | 25.0 | 25.0 | 13.1% | -0.9% | 10.1% |

**Table 1.** Five turbine results for low and high turbulence conditions using SOWFA, the Gaussian model, and the GCH model.

## 5.1 Optimization of Five Turbine Array

Engineering wake models in FLORIS are often used to determine optimal setpoints for wake steering and assess the performance of these setpoints. The results of optimizing the Gaussian and GCH models are compared in this section. Specifically, the Gaussian and GCH models were optimized individually for the five turbine case under low and high turbulence conditions. These yaw angles from each optimization were simulated in SOWFA. The power predicted in SOWFA, the Gaussian model, and the GCH model, for each set of yaw angles, are compared in Table 1. The results are compared to 1) a baseline where the yaw angles of all turbines in the five turbine array are zero, and 2) a naive strategy of simply maximizing yaw offsets, subject to an upper bound of 25° to limit structural loads, for all turbines except the last.

In both low and high turbulence cases, the GCH optimized yaw angles produced higher power gains in SOWFA compared with the Gaussian model, and also outperformed simply operating all turbines (except the last turbine) at a maximum yaw angle of 25°. Similarly to results observed in a wind tunnel study in Bastankhah and Porté-Agel (2019), GCH produces decreasing yaw angles at farther downstream turbines indicating that GCH is taking advantage of the effective yaw angle produced by the counter-rotating vortices generated by upstream turbines. Note that GCH more closely predicts the gain observed in SOWFA versus the Gaussian in all cases.

# 6   Wind Farm Analysis
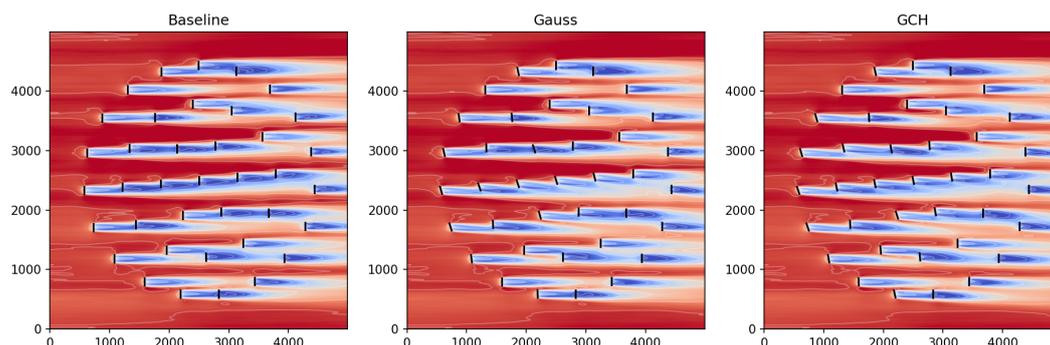
**Figure 12.** Flow field results from SOWFA where the wind direction is 270° (Case 2). The left plot shows the baseline case with all turbines aligned with the flow. The middle plot shows the flow field with yaw angles from the optimized Gaussian model and the right plot shows the flow field with the yaw angles from the optimized GCH model.

Finally, a full wind farm analysis was performed to quantify the potential of wake steering when effects such as yaw-added recovery and secondary steering are included. For this analysis, we used a 38-turbine wind farm used as in Thomas et al. (2019). The flow field for the baseline case is shown on the left in Fig. 12 where the wind direction is 270° and all turbines

5   are aligned with the flow. The middle plot shows the flow field with yaw angles from the optimized Gaussian model and the right plot shows the flow field with the yaw angles from the optimized GCH model. The analysis was performed for two wind directions, 95° and 270°, and will be referred to as Case 1 and Case 2 respectively.
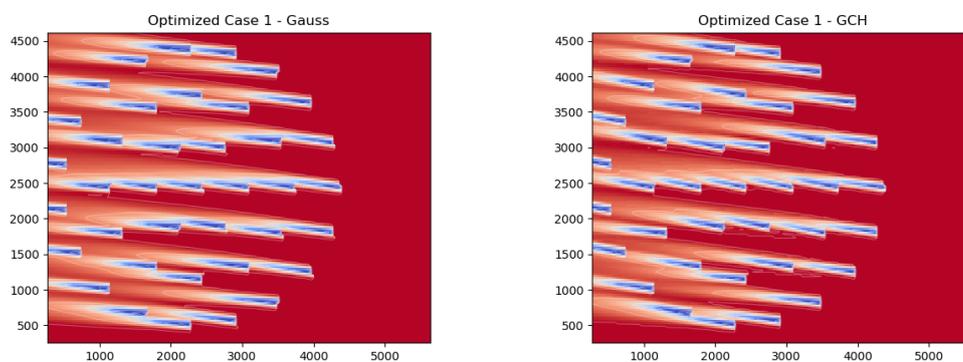
**Figure 13.** Flow fields of the optimized Gaussian model (left) and the optimized GCH model (right) for Case 1 where the wind direction is at 95°.
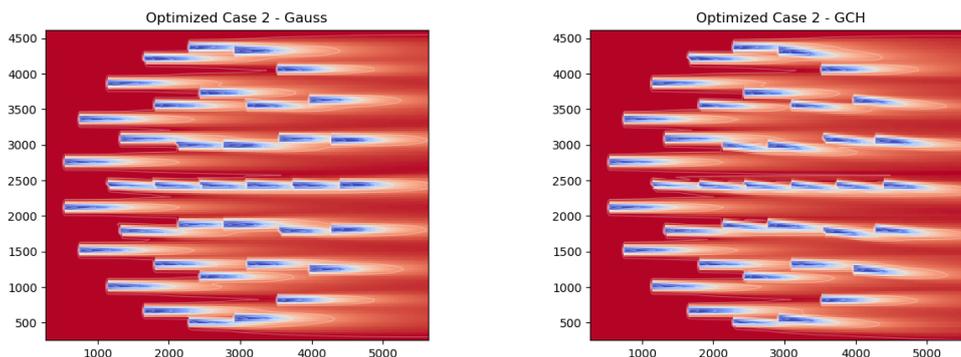
**Figure 14.** Flow fields of the optimized Gaussian model (left) and the optimized GCH model (right) for Case 2 where the wind direction is at 270°.

| Case | SOWFA Total Power Gain | Gauss Total Power Gain | GCH Total Power Gain |
|---|---|---|---|
| Low Turbulence | | | |
| Case 1 - Gauss optimized angles | 7.6% | 5.2% | 7.7% |
| Case 1 - GCH optimized angles | **8.0**% | 4.7% | 8.5% |
| Case 2 - Gauss optimized angles | 3.8% | 2.6% | 5.0% |
| Case 2 - GCH optimized angles | **4.3**% | 1.7% | 5.8% |
| High Turbulence | | | |
| Case 1 - Gauss optimized angles | 4.4% | 2.1% | 5.4% |
| Case 1 - GCH optimized angles | **4.5**% | 1.6% | 5.8% |
| Case 2 - Gauss optimized angles | 2.3% | 0.5% | 2.8% |
| Case 2 - GCH optimized angles | **3.1**% | 0.0% | 3.3% |

**Table 2.** Wind farm results for low and high turbulence conditions for SOWFA, the Gaussian model, and the GCH model.

Optimizations were performed with the Gaussian model and the GCH model for low (6%) and high (10%) turbulence conditions. Flow fields are shown in Fig. 13 for the Gaussian model (left) and the GCH model (right) for Case 1 of 95° and Fig. 14 shows the Gaussian (left) and GCH (right) model for Case 2 of 270° (bottom) under low turbulence conditions.

The results of the optimization are shown in Table 2. The optimized yaw angles from the Gaussian model and the GCH model were tested in SOWFA. As with the five turbine case, the yaw angles produced in the optimization with the GCH model had the largest gain in SOWFA. In addition, the gains computed by the GCH model are closer to the gains in the SOWFA results than the Gaussian model indicating that the GCH model is better able to capture the secondary effects of the large-scale flow structures generated by misaligned turbines.

Lastly, a full optimization over a wind rose was run for the wind farm in low and high turbulence conditions. The wind rose is shown in Fig. 15 to compute annual energy production (AEP). The Gaussian model and the GCH model were optimized for wake steering over this wind rose and the AEP gains are reported in . Table 3. The Gaussian model predictions of AEP gains are less than half of the gains predicted by the GCH model under both low and high turbulence conditions. This is a promising result for understanding the full potential of wake steering in large wind farms. By taking advantage of these large-scale flow structures, there is more potential for increasing the power production in a wind farm.
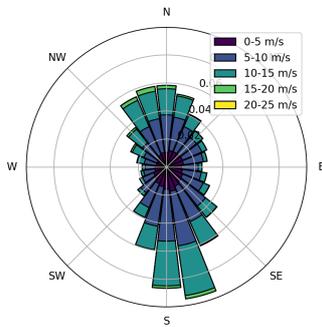
**Figure 15.** Wind rose used to compute the AEP gains from wake steering.

| Annual Energy Production Results | | |
|---|---|---|
| Model | Low Turbulence, TI = 6.5% | High Turbulence, TI = 9% |
| Gauss | 1.3% | 0.7% |
| GCH | 2.8% | 2.1% |

**Table 3.** Wind farm AEP results for low and high turbulence.

# 7 Conclusion

This paper introduces an analytical model that better captures the secondary effects of wake steering in a large wind farm. These secondary effects include yaw-added wake recovery as well as secondary wake steering that significantly boosts the impact of wake steering. The results of this model were compared with LES for two, three, and five turbine arrays as well as a 38-turbine

5     wind farm. The model compared well with results from LES and outperformed the Gaussian model in most cases. Furthermore, this paper demonstrated the possible gains in a large wind farm when considering these large-scale flow structures. Controllers can be developed in the future to manipulate these flow structures to significantly improve the performance of a wind farm.

*Acknowledgements.* This work was authored [in part] by the National Renewable Energy Laboratory, operated by Alliance for Sustainable Energy, LLC, for the U.S. Department of Energy (DOE) under Contract No. DE-AC36-08GO28308. Funding provided by the U.S. Depart-

10     ment of Energy Office of Energy Efficiency and Renewable Energy Wind Energy Technologies Office. The views expressed in the article do not necessarily represent the views of the DOE or the U.S. Government. The U.S. Government retains and the publisher, by accepting the article for publication, acknowledges that the U.S. Government retains a nonexclusive, paid-up, irrevocable, worldwide license to publish or reproduce the published form of this work, or allow others to do so, for U.S. Government purposes.

# References

Abkar, M. and Porté-Agel, F.: The effect of atmospheric stability on wind-turbine wakes: A large-eddy simulation studys, in: The Science of Making Torque from Wind, Lyngby, Denmark, 2014.

Abkar, M. and Port-Agel, F.: Influence of atmospheric stability on wind-turbine wakes: A large-eddy simulation study, Physics of Fluids, 27, doi:10.1063/1.4913695, 2015.

Annoni, J., Fleming, P., Scholbrock, A., Roadman, J., Dana, S., Adcock, C., Porte-Agel, F., Raach, S., Haizmann, F., and Schlipf, D.: Analysis of Control-Oriented Wake Modeling Tools Using Lidar Field Results, Wind Energy Science Discussions, 2018, 1–17, doi:10.5194/wes-2018-6, https://www.wind-energ-sci-discuss.net/wes-2018-6/, 2018.

Annoni, J., Dall'Anese, E., Hong, M., and Bay, C. J.: Efficient Distributed Optimization of Wind Farms Using Proximal Primal-Dual Algorithms, in: 2019 American Control Conference (ACC), pp. 4173–4178, IEEE, 2019.

Bastankhah, M. and Porté-Agel, F.: Wind farm power optimization via yaw angle control: A wind tunnel study, Journal of Renewable and Sustainable Energy, 11, 023 301, 2019.

Bastankhah, M. and Porté-Agel, F.: A new analytical model for wind-turbine wakes, Renewable Energy, 70, 116–123, 2014.

Bastankhah, M. and Porté-Agel, F.: Experimental and theoretical study of wind turbine wakes in yawed conditions, Journal of Fluid Mechanics, 806, 506–541, 2016.

Bay, C. J., Annoni, J., Martínez-Tossas, L. A., Pao, L. Y., and Johnson, K. E.: Flow Control Leveraging Downwind Rotors for Improved Wind Power Plant Operation, in: 2019 American Control Conference (ACC), pp. 2843–2848, IEEE, 2019.

Churchfield, M. J., Lundquist, J. K., Quon, E., Lee, S., and Clifton, A.: Large-Eddy Simulations of Wind Turbine Wakes Subject to Different Atmospheric Stabilities, in: American Geophysical Union Fall Meeting, 2014.

Ciri, U., Rotea, M. A., and Leonardi, S.: Effect of the turbine scale on yaw control, Wind Energy, 21, 1395–1405, 2018.

Damiani, R., Dana, S., Annoni, J., Fleming, P., Roadman, J., van Dam, J., and Dykes, K.: Assessment of Wind Turbine Component Loads Under Yaw-Offset Conditions, Wind Energy Science Discussions, 2017, 1–25, doi:10.5194/wes-2017-38, https://www.wind-energ-sci-discuss.net/wes-2017-38/, 2017.

Fleming, P., Aho, J., Gebraad, P., Pao, L., and Zhang, Y.: CFD Simulation Study of Active Power Control in Wind Plants, in: American Control Conference, 2016.

25

Fleming, P., Annoni, J., Churchfield, M., Martinez-Tossas, L. A., Gruchalla, K., Lawson, M., and Moriarty, P.: A simulation study demonstrating the importance of large-scale trailing vortices in wake steering, Wind Energy Science, 3, 243–255, doi:10.5194/wes-3-243-2018, https://www.wind-energ-sci.net/3/243/2018/, 2018a.

Fleming, P., Annoni, J., Martínez-Tossas, L. A., Raach, S., Gruchalla, K., Andrew Scholbrock, Churchfield, M., and Roadman, J.: Investigation into the shape of a wake of a yawed full-scale turbine, Journal of Physics: Conference Series, 1037, 032 010, http://stacks.iop.org/1742-6596/1037/i=3/a=032010, 2018b.

30

Fleming, P., King, J., Dykes, K., Simley, E., Roadman, J., Scholbrock, A., Murphy, P., Lundquist, J. K., Moriarty, P., Fleming, K., van Dam, J., Bay, C., Mudafort, R., Lopez, H., Skopek, J., Scott, M., Ryan, B., Guernsey, C., and Brake, D.: Initial results from a field campaign of wake steering applied at a commercial wind farm – Part 1, Wind Energy Science, 4, 273–285, doi:10.5194/wes-4-273-2019, https://www.wind-energ-sci.net/4/273/2019/, 2019a.

35

Fleming, P., King, J., Simley, E., Roadman, J., Scholbrock, A., Murphy, P., Lundquist, J. K., Moriarty, P., Fleming, K., van Dam, J., Bay, C., Mudafort, R., Lopez, H., Skopek, J., Scott, M., Ryan, B., Guernsey, C., and Brake, D.: Continued Results from a Field Campaign of Wake Steering Applied at a Commercial Wind Farm: Part 2, Submitted to Wind Energy Science, 2019b.

Gebraad, P., Teeuwisse, F., Wingerden, J., Fleming, P. A., Ruben, S., Marden, J., and Pao, L.: Wind plant power optimization through yaw control using a parametric model for wake effects—a CFD simulation study, Wind Energy, 19, 95–114, 2016.

Gebraad, P., Thomas, J. J., Ning, A., Fleming, P., and Dykes, K.: Maximization of the annual energy production of wind power plants by optimization of layout and yaw-based wake control, Wind Energy, 20, 97–107, 2017.

Howland, M. F., Bossuyt, J., Martínez-Tossas, L. A., Meyers, J., and Meneveau, C.: Wake structure in actuator disk models of wind turbines in yaw under uniform inflow conditions, Journal of Renewable and Sustainable Energy, 8, 043 301, doi:10.1063/1.4955091, 2016.

Jensen, N. O.: A note on wind generator interaction, Tech. Rep. Risø-M-2411, Risø National Laboratory, 1984.

Jiménez, Á., Crespo, A., and Migoya, E.: Application of a LES technique to characterize the wake deflection of a wind turbine in yaw, Wind energy, 13, 559–572, 2010.

Katić, I., Højstrup, J., and Jensen, N. O.: A simple model for cluster efficiency, in: EWEA Conference and Exhibition, pp. 407–410, Rome, Italy, 1986.

Martínez-Tossas, L. A., Annoni, J., Fleming, P. A., and Churchfield, M. J.: The aerodynamics of the curled wake: a simplified model in view of flow control, Wind Energy Science (Online), 4, 2019.

Martínez-Tossas, L. A., Churchfield, M. J., and Leonardi, S.: Large eddy simulations of the flow past wind turbines: actuator line and disk modeling, Wind Energy, 18, 1047–1060, 2015.

Medici, D. and Alfredsson, P.: Measurements on a wind turbine wake: 3D effects and bluff body vortex shedding, Wind Energy, 9, 219–236, 2006.

Niayifar, A. and Porté-Agel, F.: A new analytical model for wind farm power prediction, in: Journal of Physics: Conference Series, vol. 625, p. 012039, IOP Publishing, 2015.

NREL: FLORIS. Version 1.1.4, https://github.com/NREL/floris, 2019.

Pope, S. B.: Turbulent flows, 2001.

Schottler, J., Hölling, A., Peinke, J., and Hölling, M.: Wind tunnel tests on controllable model wind turbines in yaw, in: 34th Wind Energy Symposium, p. 1523, 2016.

Shapiro, C. R., Gayme, D. F., and Meneveau, C.: Modelling yawed wind turbine wakes: a lifting line approach, Journal of Fluid Mechanics, 841, 2018.

Simley, E., Fleming, P., and King, J.: Design and Analysis of a Wake Steering Controller with Wind Direction Variability, Wind Energy Science Discussions, 2019, 1–26, doi:10.5194/wes-2019-35, https://www.wind-energ-sci-discuss.net/wes-2019-35/, 2019.

Stanley, A. P. J. and Ning, A.: Massive Simplification of the Wind Farm Layout Optimization Problem, Wind Energy Science Discussions, 2019, 1–20, doi:10.5194/wes-2019-37, https://www.wind-energ-sci-discuss.net/wes-2019-37/, 2019.

Thomas, J. J., Annoni, J., Fleming, P. A., and Ning, A.: Comparison of Wind Farm Layout Optimization Results Using a Simple Wake Model and Gradient-Based Optimization to Large Eddy Simulations, in: AIAA Scitech 2019 Forum, p. 0538, 2019.

Vollmer, L., Steinfeld, G., Heinemann, D., and Kühn, M.: Estimating the wake deflection downstream of a wind turbine in different atmospheric stabilities: an LES study, Wind Energy Science, 1, 129–141, 2016.

Wagenaar, J., Machielse, L., and Schepers, J.: Controlling wind in ECN's scaled wind farm, Proc. Europe Premier Wind Energy Event, pp. 685–694, 2012.